A Chain-Weaver Balanced Power Amplifier With an Embedded Impedance/Power Sensor

Pashaeifar, Masoud; Kumaran, Anil Kumar; De Vreede, Leo C.N.; Alavi, Morteza S.

DOI
10.1109/JSSC.2024.3453213

Publication date
2024

Document Version
Final published version

Published in
IEEE Journal of Solid-State Circuits

A Chain-Weaver Balanced Power Amplifier With an Embedded Impedance/Power Sensor

Masoud Pashaeifar, *Member, IEEE*, Anil Kumar Kumaran, *Graduate Student Member, IEEE*, Leo C. N. de Vreede, *Senior Member, IEEE*, and Morteza S. Alavi, *Senior Member, IEEE*

***Abstract*— This article introduces an *N*-way chain-weaver balanced power amplifier (PA) for millimeter-wave (mm-wave) phased-array transmitters (TXs). Taking advantage of the proposed combining network, an embedded impedance/power sensor is implemented, which can be utilized for output power regulation, built-in self-test, and load-based performance optimization. The proposed PA architecture offers linearity and gain robustness under the antenna's frequency/time-dependent voltage standing wave ratio (VSWR). In the event of impedance mismatch, the proposed PA provides *N* different loads equally distributed on the VSWR circle. Consequently, the performance of the PAs is the average of *N* PAs with *N* different loads, which makes this structure VSWR resilient. As a proof of concept, an eight-way chain-weaver balanced PA (BPA) is realized in 40-nm bulk CMOS technology, and it delivers 25.19-dBm P_{SAT} with 16.19% PAE. The proposed PA supports a 2-GHz 64-QAM OFDM signal with 16-dBm average power, achieving −25-dB error vector magnitude (EVM). The average EVM is better than −30.3 dB without digital pre-distortion (DPD) for an "800-MHz 256-QAM OFDM" signal while generating an average output power of 12.17 dBm. The performance of the PA is also evaluated under 1.5:1–3:1 VSWR conditions. The measured small-signal gain variation under VSWR 3:1 is ±0.7 dB. Moreover, assuming any frequency/time-dependent loading condition within the VSWR 3:1 circle, the proposed chain-weaver BPA achieves <2.8° amplitude-to-phase (AM–PM) over 3-GHz bandwidth. Besides, the embedded impedance/power sensor accuracy outperforms the state of the art. The proposed impedance sensor can measure VSWR 3:1 by the maximum angle and magnitude errors of 12.3° and 0.106, respectively.**

***Index Terms*— 5G, amplitude-to-amplitude (AM–AM), amplitude-to-phase (AM–PM), balanced power amplifier, chain weaver, impedance sensor, mutual coupling, power amplifier (PA), power sensor, quadrature hybrid coupler, rms detector (DET), transmission line (TL), voltage standing wave ratio (VSWR), wideband.**

I. Introduction

POWER amplifiers (PAs) are one of the crucial parts of the millimeter-wave (mm-wave) 5G transmitters (TXs), as they usually define the TX linearity, reliability, and efficiency. Taking advantage of the mm-wave phased-array architecture empowers 5G TXs to achieve the required equivalent isotropic radiated power (EIRP) with a reasonable average output power levels, e.g., 9 dBm for backhaul and 15 dBm for handset applications [1]. On the other hand, they typically employ spectrally efficient complex modulation schemes with high peak-to-average-power ratios (PAPRs), e.g., 11 dB [2]. Besides, in the hybrid/analog beamforming architectures, the TX signal reaches the PA's input with a low power level due to losses of preceding stages, including power splitters and phase shifters [3]. Therefore, the PA must provide a high gain and peak output power to achieve the required average EIRP.

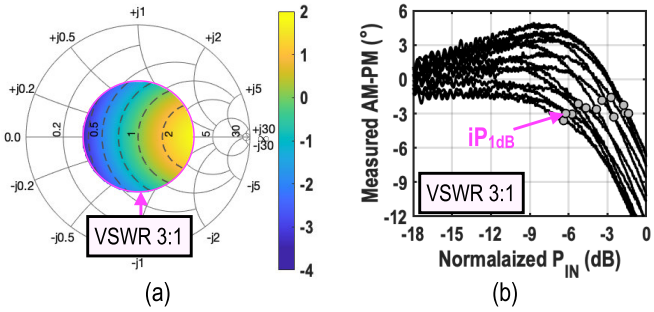

Fig. 1. (a) Simulated gain variation of a single-branch PA with $\Gamma_{OUT} = -4$ dB. (b) Measured $iP_{1\,dB}$ and AM–PM of a 40-nm CMOS linear PA [4] at 28.5 GHz under a VSWR of 3:1 with various VSWR angles.

Moreover, the TX must satisfy the ever-tightening linearity specifications of the 5G systems, verified by the error vector magnitude (EVM). Among all noise and non-linearity contributors of an mm-wave TX, the PA typically owns most of the EVM budget, as it must handle a large signal while directly interfacing with the antenna [5]. Hence, several mm-wave linear PAs have been introduced to address the 5G EVM specifications [6], [7], [8], [9], [10], [11], [12], [13], [14], [15], [16], [17], [18], [19], [20], [21]. Nevertheless, the critical challenge is achieving the required gain, power, and EVM and maintaining them over the voltage standing wave ratio (VSWR) provided by the antenna and its connection [22]. Fig. 1(a) exhibits the simulated gain variation of a single-branch PA ($\Gamma_{OUT} = -4$ dB) for VSWR <3:1. It shows more than 5-dB gain variation, while only 1.249 dB comes from load mismatch loss ($1-|\Gamma_L|^2$). Furthermore, assuming no memory effect, the EVM of a PA can be directly determined by its amplitude-to-amplitude (AM–AM) and amplitude-to-phase (AM–PM) distortions. Fig. 1(b) demonstrates the measured input 1-dB compression point ($iP_{1\,dB}$) and AM–PM of a 40-nm CMOS linear PA [4] at 28.5 GHz under the VSWR

Manuscript received 29 April 2024; revised 4 August 2024 and 18 August 2024; accepted 23 August 2024. Date of publication 13 September 2024; date of current version 25 November 2024. This article was approved by Associate Editor Wei Deng. This work was supported by the NWO/NXP 5G Partnership under Project 15593. *(Corresponding author: Masoud Pashaeifar.)*

The authors are with the Department of Microelectronics, Delft University of Technology, 2628 CD Delft, The Netherlands (e-mail: m.pashaeifar@tudelft.nl).

Color versions of one or more figures in this article are available at https://doi.org/10.1109/JSSC.2024.3453213.

Digital Object Identifier 10.1109/JSSC.2024.3453213

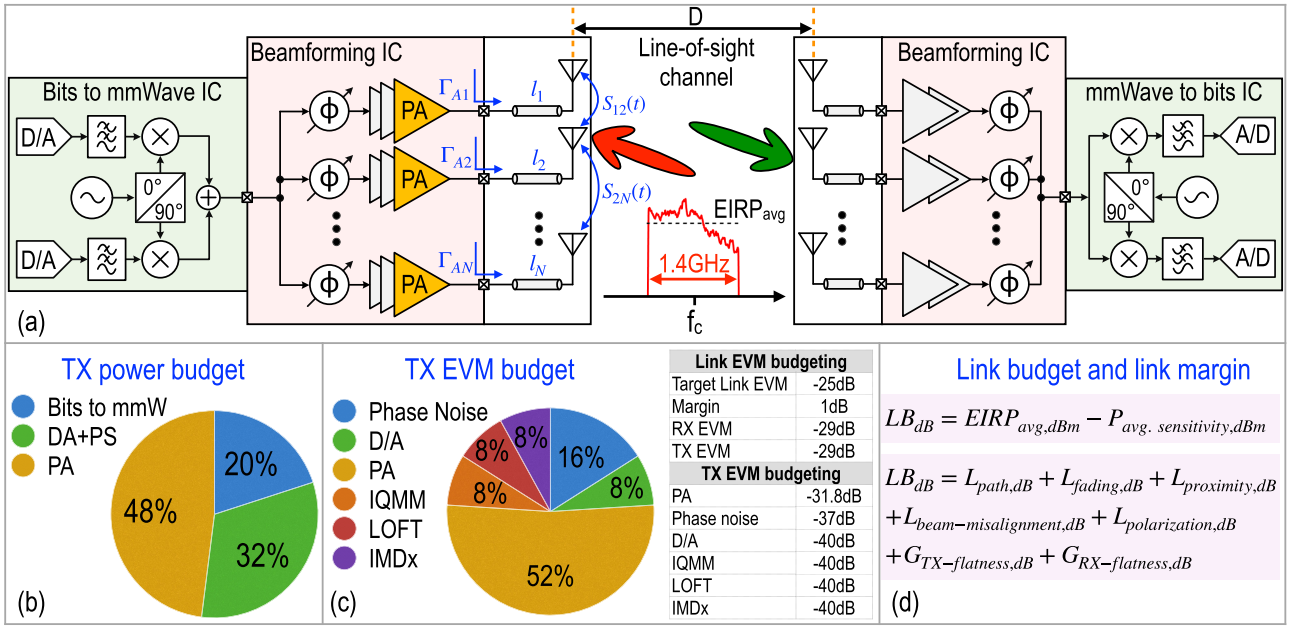

Fig. 2. (a) Simplified phased-array link supporting up to 1.4-GHz modulation bandwidth. The PAs share TX's (b) power and (c) EVM budgets. (d) Link budget calculation taking into account the TX/RX gain flatness.

of 3:1. It shows more than 5-dB iP$_{1\,dB}$ variation over various VSWR angles, while its AM–PM at input power <iP$_{1\,dB}$ fluctuates between $-3.7°$ and 5°.

Since the mm-wave 5G TXs must support modulation bandwidths up to 1.4 GHz, the antenna impedance can vary significantly over such a large bandwidth [23]. This dependency becomes more complex when considering a time-varying VSWR caused by the beam-angle-dependent element-to-element mutual coupling of the phased-array TX and environmental changes [24], [25], [26], [27], [28]. This time- and frequency-dependent VSWR deteriorates PA gain flatness, output 1-dB compression point (oP$_{1\,dB}$), AM–AM, AM–PM, and reliability. The gain-flatness correction consumes the link budget, while the PA needs to be over-dimensioned to satisfy the required EIRP, linearity, and reliability over the signal bandwidth to handle the worst case (wc) VSWR scenario.

Active load-pulling and reconfigurable matching networks are introduced to address the VSWR issue [29], [30], [31]. However, since the PA can be tuned only for a specific antenna impedance (i.e., at a chosen frequency), reconfigurable matching networks do not offer frequency-dependent VSWR compensation. A conventional solution for a VSWR-resilient PA is employing an isolator at its output. Unfortunately, due to the area constraint of the phased-array transceivers, an integrated isolator would not be a viable solution. Moreover, despite the development of integrated state-of-the-art mm-waves isolators [4], [32], [33], they yield area overhead, demonstrate high TX-to-antenna loss (>1.8 dB), and require extra power consumption to generate their quadrature clocks. In addition, a VSWR-resilient impedance/power sensor is an essential part of such a PA to regulate gain, beam pattern, and EIRP [34], [35], [36], [37].

On the other hand, balanced PAs (BPAs) provide inherent VSWR resilience by relying on the cancellation of the reflected wave [38]. This article introduces the chain-weaver BPA architecture [39] extending the conventional BPA's linearity, gain, and power resilience under significant frequency- and time-dependent VSWRs. The proposed mm-wave PA features: 1) a four-stage eight-way power-combined Class-AB PA achieving high output power, gain, and linearity; 2) a chain-weaver balanced power combiner for VSWR resilience; and 3) an embedded impedance/power sensor.

This article is organized as follows. Section II discusses phased-array link system considerations and requirements for PA designing. The proposed chain-weaver BPA architecture is introduced in Section III. Section IV presents the proposed embedded impedance/power sensor. Section V elaborates on circuit implementation details of the chain-weaver BPA prototype fabricated in the 40-nm bulk CMOS technology. Section VI presents the experimental results of the chain-weaver PA, while the measurement results of the impedance/power sensor are discussed in Section VII. Finally, we conclude our work in Section VIII.

II. System Considerations and Requirements

In this section, we discuss the PA design considerations when the optimization goal is the communication link power consumption, not PAE. Fig. 2(a) demonstrates a simplified phased-array link supporting up to 1.4-GHz modulation bandwidth as the front-end component in the TX beamforming IC, and the PAs face the impedance presented by the antenna arrays. As depicted, due to different connection lengths, the PAs see unequal frequency-dependent load impedance and connection loss. In addition, the beam-angle-dependent element-to-element mutual coupling adds a time-dependent factor to the VSWR experienced by the PAs. Furthermore, human body proximity and environmental changes, although at a lower rate, affect the impedance seen by the PAs.

As depicted in Fig. 1, VSWR variation influences the gain, output compression power levels, and linearity. Therefore, frequency-dependent VSWR leads to gain, power, and EVM deviation over frequency within the modulation bandwidth. This imposes many design challenges through the link and increases total power consumption. For instance, the PA must deliver an average output power (P_{AVG}) to support the specified EIRP. Hence, the required peak power (P_{Peak}) in the presence of VSWR can be calculated as

$$P_{\text{Peak}} = P_{\text{AVG}} + \text{PAPR} + \Delta P \tag{1}$$

where ΔP represents the difference between the wc and 50-Ω peak power ($P_{\text{Peak-wc}} - P_{\text{Peak-50}\,\Omega}$) for all possible VSWR condition. Assuming an ideal class B PA, $\Delta P = 1$ dB degrades the average PAE by $\times 0.8$. Fig. 2(b) depicts an example power consumption budget of a phased-array TX, introducing the PAs as the dominant power consumer. This power consumption budget is estimated based on information reported in [16], [40], and [41], assuming that beam-forming IC consists of 16 beam-forming elements and PAs can deliver 20-dBm peak power with 30% efficiency with a Class-B-like efficiency curve. Although a highly efficient PA architecture can optimize the power budget [42], [43], [44], [45], [46], a VSWR-resilient PA will prevent the need for over-designing, yielding a reduced power consumption.

In general, EVM budgeting can significantly affect the power consumption budget and, thus, the total power consumption. The following equation can estimate the overall EVM of the TX:

$$\text{EVM}_{\text{TX}} = \sqrt{\text{EVM}_{\text{D/A}}^2 + \text{EVM}_{\text{UC}}^2 + \text{EVM}_{\text{IMDx}}^2 + \text{EVM}_{\text{PA}}^2} \tag{2}$$

and

$$\text{EVM}_{\text{UC}} = \sqrt{\text{EVM}_{\text{P.N}}^2 + \text{EVM}_{\text{IQMM}}^2 + \text{EVM}_{\text{LOFT}}^2} \tag{3}$$

where $\text{EVM}_{\text{D/A}}$, EVM_{UC}, EVM_{IMDx}, and EVM_{PA} are the EVM degraded by quantization noise, up-conversion, odd/even order distortions, and the PA non-linearity, respectively. Also, the up-conversion EVM contribution includes $\text{EVM}_{\text{P.N.}}$, EVM_{IQMM}, and EVM_{LOFT}, which are contributions of phase noise, I/Q modulation imbalance, and LO feed through (LOFT), respectively.

Targeting −25-dB EVM with 1-dB margin and assuming an equal contribution for RX and TX, Fig. 2(c) exhibits a simplified EVM budget example of the TX calculated based on performance reported in [16], [40], [41], [47], [48], and [49]. Here, we assume −37-dB phase noise contribution and −40 dB for in-phase quadrature mismatch (IQMM), LOFT, quantization noise, and odd-/even-order distortions. The most significant portion of the TX EVM budget is given to the PA as it usually bottlenecks in TX's linearity and power consumption. Furthermore, as shown in Fig. 1(b), VSWR significantly influences PA EVM. This feature enforces the choice of less efficient PA operation, exploiting more linear biasing conditions and over-designing. In addition, the PA might require a larger EVM budget, thus tightening the other blocks' linearity specifications and increasing the total power consumption.

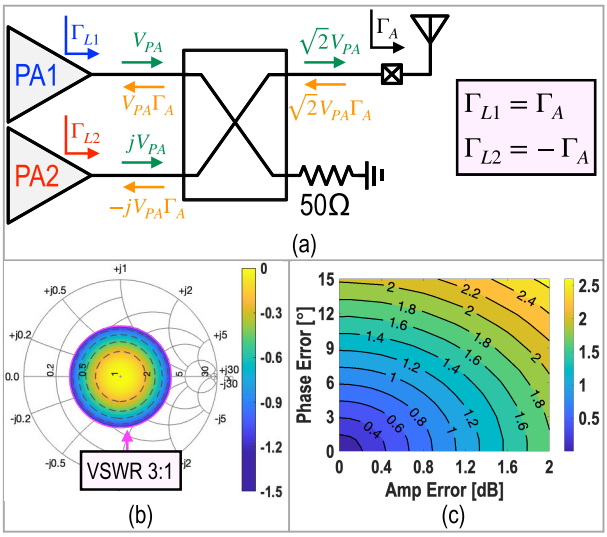

Fig. 3. (a) Simplified block diagram of the BPA and its forward and reflected waves assuming matched PA units ($\Gamma_{\text{PA}} = 0$). (b) Gain of the BPA assuming ideal QHC. (c) Gain variation of the BPA over VSWR 3:1 circle versus amplitude and phase error of the QHC.

Finally, the link budget calculation is presented in Fig. 2(d), considering the TX/RX gain flatness. The frequency-dependent VSWR results in a frequency-dependent gain and EVM, which requires a higher EVM to satisfy the link budget. Therefore, over-designing at the link level is typically essential to address the required link budget, imposing higher link power consumption.

III. Chain-Weaver BPA

This section discusses an N-way combining solution that can provide inherent resilience against frequency- and time-dependent VSWRs.

A. Conventional BPA

BPA provides inherent VSWR resilience by relying on the cancellation of the reflected wave [5], [50], [51], [52]. It consists of two PAs combined by an isolated quadrature combiner. The quadrature combiner can be implemented with a two-way Wilkinson power combiner, where one of the PAs is connected to the combiner by a $\lambda/4$ transmission lines (TLs) [50]. An alternative quadrature combiner is, as depicted in Fig. 3(a), a quadrature-hybrid coupler (QHC). The forward and reflected waves shown in Fig. 3(a) imply that the reflection coefficient seen by the PAs is 180° out of phase. Here, the PAs are considered as matched ports for simplification. Therefore, any reflected waves from the antenna do not influence the forward power of the PAs and, consequently, that of the BPA. Nonetheless, as discussed in [5], the BPA provides broadband output matching independent of PAs' impedance. This output matching alleviates the gain variation under the frequency-dependent VSWR. In Fig. 3(b), the gain variation of a BPA under VSWR is demonstrated, which is only <1.249 dB due to mismatch loss of the antenna ($1-|\Gamma|^2$). However, as shown in Fig. 3(c), the relative gain deviation of the BPA moving on VSWR 3:1 circle heavily depends on the QHC amplitude and phase error.

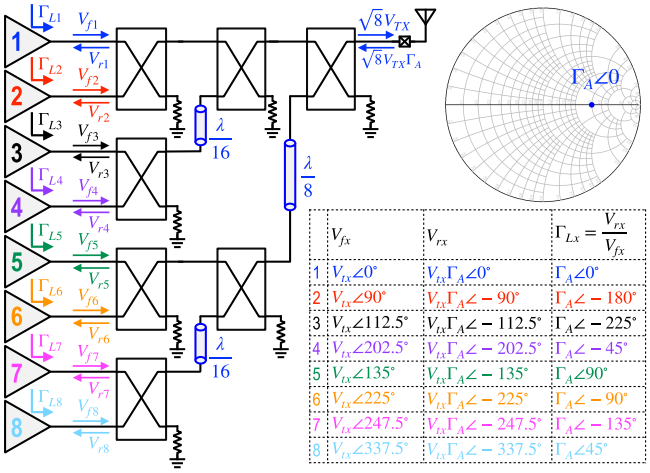

	V_{fx}	V_{rx}	$\Gamma_{Lx}=\frac{V_{rx}}{V_{fx}}$
1	$V_{tx}\angle 0°$	$V_{tx}\Gamma_A\angle 0°$	$\Gamma_A\angle 0°$
2	$V_{tx}\angle 90°$	$V_{tx}\Gamma_A\angle -90°$	$\Gamma_A\angle -180°$
3	$V_{tx}\angle 112.5°$	$V_{tx}\Gamma_A\angle -112.5°$	$\Gamma_A\angle -225°$
4	$V_{tx}\angle 202.5°$	$V_{tx}\Gamma_A\angle -202.5°$	$\Gamma_A\angle -45°$
5	$V_{tx}\angle 135°$	$V_{tx}\Gamma_A\angle -135°$	$\Gamma_A\angle 90°$
6	$V_{tx}\angle 225°$	$V_{tx}\Gamma_A\angle -225°$	$\Gamma_A\angle -90°$
7	$V_{tx}\angle 247.5°$	$V_{tx}\Gamma_A\angle -247.5°$	$\Gamma_A\angle -135°$
8	$V_{tx}\angle 337.5°$	$V_{tx}\Gamma_A\angle -337.5°$	$\Gamma_A\angle 45°$

Fig. 4. Simplified block diagram of an eight-way BPA and its forward and reflected waves assuming matched PA units ($\Gamma_{PA}=0$).

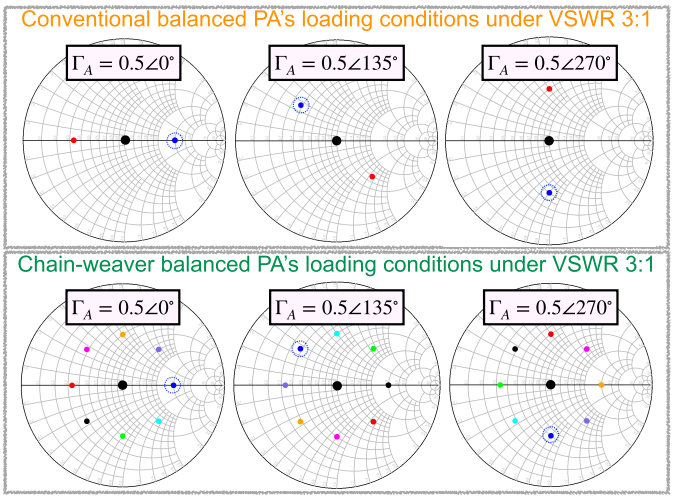

Fig. 5. Loading condition of the conventional BPA and eighth-way chain-weaver PA under VSWR 3:1.

B. Chain-Weaver BPA

Moving on a VSWR circle with 1° increment, a single-branch PA sees 360 different loading conditions leading to performance variation. BPA, on the other hand, provides 180 different loading conditions for its PAs as one sees the inverted load of the other. In addition, in this 180 loading condition, the overall performance is the average of two PAs with opposite loads, leading to a more robust performance over VSWR angles. To further extend the VSWR resilience of the BPA, we proposed the chain-weaver BPA. The goal is to introduce an N-way power combiner, which offers $(360/N)$ different loading conditions for N PAs.

The proposed N-way chain-weaver BPA is demonstrated in Fig. 4, where $N=8$. The chain-weaver BPA consists of eight equally weighted PAs combined in three stages. In the first stage, four QHCs are employed as two-way isolated quadrature power combiners, where two $\lambda/16$ TLs are added to the output of two of them, providing 22.5° phase shift for both forward and reflected signals. The second stage comprises two QHCs and one $\lambda/8$ TL at the output of one of them for a 45° phase shift. Finally, the third stage is a QHC directly connected to the antenna port. In this combining structure, the $\lambda/16$ and $\lambda/8$ TLs provide a unique phase shift, with a 22.5° increment, from each PA to the antenna port. As presented in Fig. 4, these unique phase shifts must be included in the forward signals ($V_{\rm fx}$) for combining constructively at the antenna port, where the overall forward signal level is $\sqrt{8}V_{\rm tx}$. In the antenna load mismatch event, the reflected wave from the antenna ($\sqrt{8}V_{\rm tx}\Gamma_A$) travels back and reaches each PA with the same phase shift ($V_{\rm rx}$). Knowing the forward and reflected waves at each PA port, the reflection coefficient seen by each PA can be calculated ($\Gamma_{\rm Lx}=(V_{\rm rx}/V_{\rm fx})$). Since the combining gain from the PAs to the antenna is identical, all PAs see the same reflection coefficient magnitude. However, owing to the phase shift with a 22.5° increment, the reflection coefficient seen by each PA has a unique angle with a $(360°/8)=45°$ increment, as depicted in Fig. 4. Therefore, assuming lossless QHCs, this structure distributes the PAs' load like a chain-dotted circle on the VSWR circle with a 45° distance.

Fig. 5 demonstrates the loading conditions for VSWR 3:1 and three VSWR angles. In a conventional BPA, the PAs experience both the actual and inverted antenna impedance. Still, the loading conditions are different in these three VSWR angles, leading to linearity degradation. In the proposed chain-weaver BPA, however, only the places of the PAs are shifted in the chain-dotted circle, resulting in the same overall loading conditions. As such, assuming identical unit PAs, the gain, $oP_{1\,\rm dB}$, and linearity of the overall structure are equal for these three VSWR angles.

Thus far, the PAs are considered an ideal matched signal port with fixed forward power for simplification. However, as discussed in [5], the impedance seen by the PAs is a function of their impedance. Assuming $\Gamma_{\rm PA}$ and Γ_A as the reflection coefficient of the PAs and antenna, respectively, the load seen by eight PAs is given as follows:

$$\begin{aligned}
\Gamma_{L1}&=\frac{\Gamma_A\angle 0°}{1+\Gamma_{\rm PA}\Gamma_A\angle 0°}, \quad \Gamma_{L2}=\frac{\Gamma_A\angle -180°}{1+\Gamma_{\rm PA}\Gamma_A\angle -180°}\\
\Gamma_{L3}&=\frac{\Gamma_A\angle -225°}{1+\Gamma_{\rm PA}\Gamma_A\angle -225°}, \quad \Gamma_{L4}=\frac{\Gamma_A\angle -45°}{1+\Gamma_{\rm PA}\Gamma_A\angle -45°}\\
\Gamma_{L5}&=\frac{\Gamma_A\angle -270°}{1+\Gamma_{\rm PA}\Gamma_A\angle -270°}, \quad \Gamma_{L6}=\frac{\Gamma_A\angle -90°}{1+\Gamma_{\rm PA}\Gamma_A\angle -90°}\\
\Gamma_{L7}&=\frac{\Gamma_A\angle -135°}{1+\Gamma_{\rm PA}\Gamma_A\angle -135°}, \quad \Gamma_{L8}=\frac{\Gamma_A\angle -335°}{1+\Gamma_{\rm PA}\Gamma_A\angle -335°}.
\end{aligned} \tag{4}$$

Moreover, since the PAs are not matched, the reflected signal from the antenna will reflect and, eventually, in the steady state, will be absorbed in the first-stage QHCs' termination resistor. The absorbed signal's magnitude ($V_{\rm term}$) can be calculated as

$$V_{\rm term}=\sqrt{2}V_{\rm tx}|\Gamma_A||{\rm IL}_t|^2|{\rm IL}_{\rm QHC1}||\Gamma_{\rm PA}| \tag{5}$$

where ${\rm IL}_t$ and ${\rm IL}_{\rm QHC1}$ are the total insertion loss of the chain-weaver power combiner and the insertion loss of the first stage's QHC, respectively. Therefore, these four termination resistors' reliability criteria must be satisfied for the maximum possible VSWR. As the first stage provides matched output,

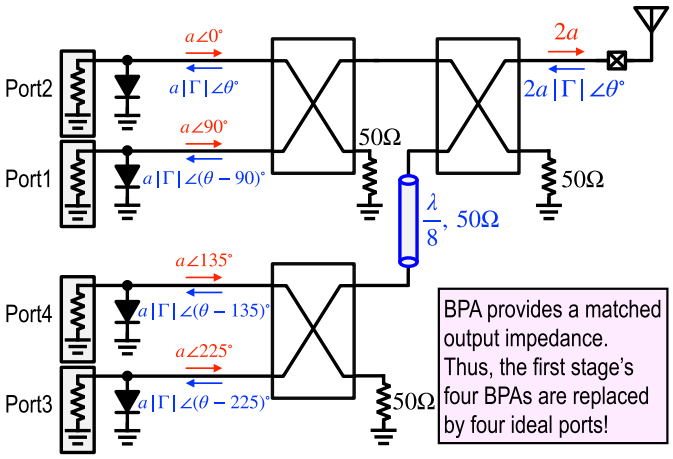

Fig. 6. Simplified schematic of the embedded VSWR-resilient impedance/power sensor.

thus completely absorbing the reflected power, the second- and third-stage termination resistors' signal is zero. However, this is only true when assuming no IQMM for the QHCs. In practice, even with the matched load, part of the power will be directed to the termination resistors due to the IQMM, which is discussed in the Appendix.

Note that a four-way Wilkinson-based power combiner/splitter with a phase shift of 45° increment is implemented in [50]. However, it is not easily scalable due to its unbalanced and asymmetrical structure.

IV. Embedded Impedance/Power Sensor

Fig. 6 unveils the simplified schematic of the embedded VSWR-resilient impedance/power sensor. Since the first-stage BPAs' output impedance is matched to the characteristic impedance of its QHC ($Z_0 = 50\ \Omega$) [5], the first-stage BPAs are considered ideal power ports. It means that the forward wave at each port is independent of the reflected wave. In Fig. 6, a is the magnitude of forward wave at each port and $\Gamma\angle\theta^\circ$ is the reflection coefficient of the antenna. As shown, an rms or peak detector (DET) can be used at each port to measure the combined voltage of the forward (V_f) and reflected (V_r) waves ($V_i^2 = |V_f + V_r|^2$). Since the port impedance and the characteristic impedance of the following QHC are 50 Ω, the combined voltage represents the combined power accordingly. Assuming an antenna reflection coefficient with magnitude and angle of $|\Gamma|$ and θ, respectively, and lossless QHCs and TL, the forward and reflected waves at four ports are presented in Fig. 6. Hence, the voltage at each port can be calculated as follows:

$$\begin{aligned} V_1^2 &= a^2(1+|\Gamma|^2-2|\Gamma|\cos\theta)\\ V_2^2 &= a^2(1+|\Gamma|^2+2|\Gamma|\cos\theta)\\ V_3^2 &= a^2(1+|\Gamma|^2-2|\Gamma|\sin\theta)\\ V_4^2 &= a^2(1+|\Gamma|^2+2|\Gamma|\sin\theta). \end{aligned} \tag{6}$$

Please note that in the conventional BPA, due to the 90° phase increment, only two of the above equations, V_1^2 and V_2^2, can be achieved, which is not sufficient for calculating impedance and power. Thanks to the chain-weaver BPA's $\lambda/8$ TL, four equations are available to calculate three unknown parameters ($|\Gamma|$, θ, and a). Although only three equations are required to calculate the unknown variables, we would calculate the impedance and power using all four voltages to minimize the effect of limited accuracy and dynamic range of the utilized rms or peak DETs. Therefore, assuming lossless passives, the angle and magnitude of the antenna can be calculated as

$$\theta = \tan^{-1}\frac{V_3^2 - V_4^2}{V_2^2 - V_1^2} \tag{7}$$

$$|\Gamma| = \frac{V_1^2+V_2^2}{V_1^2-V_2^2}\cos\theta - \sqrt{\left(\frac{V_1^2+V_2^2}{V_1^2-V_2^2}\cos\theta\right)^2 - 1}. \tag{8}$$

In addition, the delivered power to the antenna can be expressed as

$$P_{\text{Sense}} = \frac{(1-|\Gamma|^2)2a^2}{Z_0} = \frac{1-|\Gamma|^2}{(1+|\Gamma|^2)2Z_0}\sum_{i=1}^{4} V_i^2. \tag{9}$$

Thus far, the passives are considered ideal and lossless. However, the loss of the QHCs and the TL, as well as the magnitude and phase deviation of these four combining paths, affect the accuracy of the calculation. For instance, the reflected wave at the port can be derived as

$$V_{r1} = \left(\sum_{i=1}^{4} V_{fi}S_{5i}\right)S_{15}|\Gamma|\angle\theta \tag{10}$$

where V_{fi} is the forward wave of port i and S_{ji} represents the scattering parameters assuming the antenna as the fifth port. In this work, we assume an equal insertion loss in four combining paths without any magnitude and phase mismatch within them. Therefore, we use (7)–(9) to calculate the antenna impedance and output power and apply a constant coefficient correction factor for taking into account the insertion loss. This further implies that using all four equations of (6) can alleviate the inaccuracies.

Moreover, the primary limiting parameter for achieving a higher VSWR measurement range is the dynamic range of the rms or peak DETs. Assuming a perfect output-matching condition for the first stage, the maximum-to-minimum voltage swing ratio equals the VSWR. In addition, the dynamic range of the rms or peak DETs constrains the dynamic range of power sensing. Therefore, the dynamic range of rms or peak DETs must be more than 20 log VSWR to support the targeted VSWR while providing the required power-sensing dynamic range.

V. Circuit Implementation

The proposed eight-way chain-weaver BPA is realized in 40-nm bulk CMOS technology by occupying 2.08-mm^2 core area. Fig. 7 demonstrates a detailed schematic view and the die micrograph of the proposed chain-weaver BPA. Starting from the RF_{IN} port, two common-source pre-driver (PD) stages are employed to deliver the required high-power gain. Then, the amplified signal is split by a eight-way splitter, a 180° rotated version of the output power combiner. The first stage of the

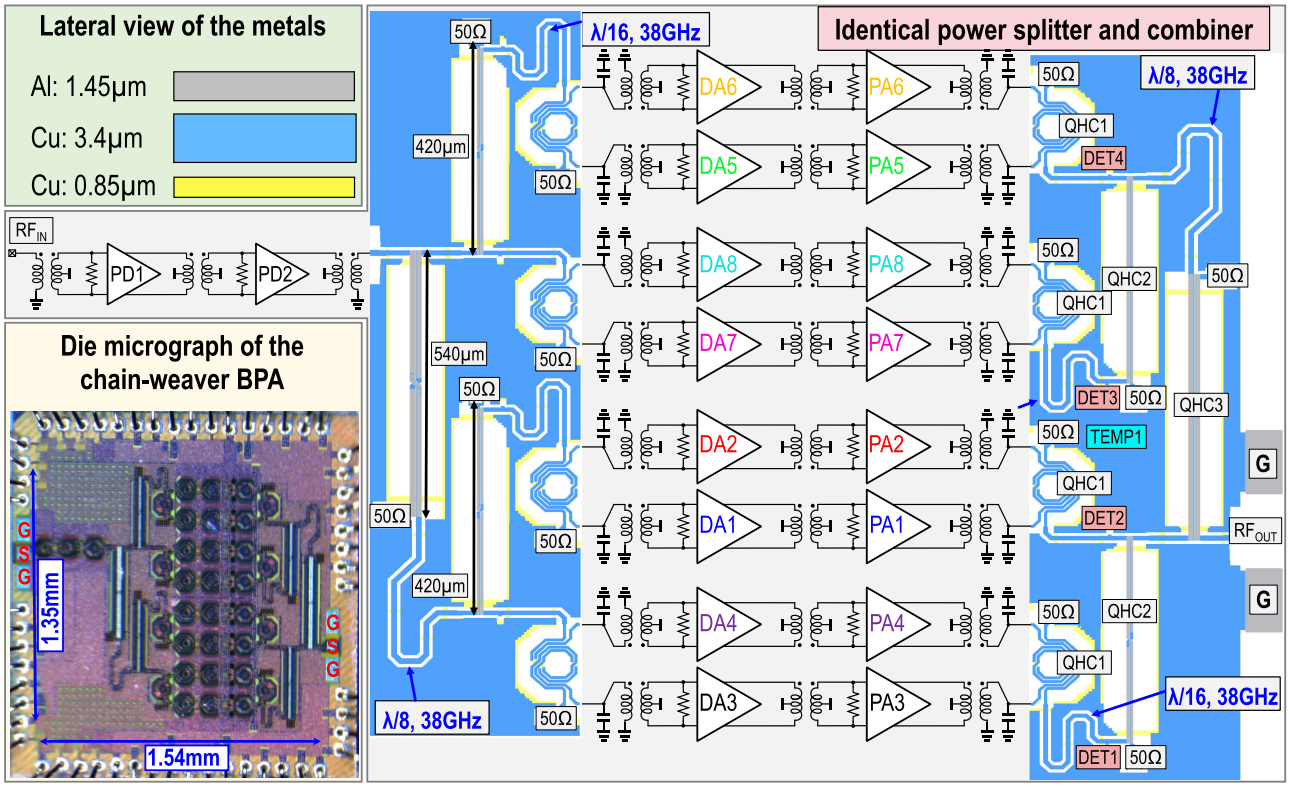

Fig. 7. Detailed schematic and die photography of the proposed eight-way chain-weaver BPA.

eight-way chain-weaver combiner comprises four identical QHCs (QHC1), forming four BPAs. QHC1 is implemented by a compact transformer-based structure for tight floor planning [5]. Besides, two $\lambda/16$ coplanar TLs connect the second and fourth QHCs' output to the second combining stage, forming the required 22.5° phase shift. Here, the reflection wave is absorbed in the termination resistors of the first stages' QHCs. As such, their reliability for the wc VSWR condition must be satisfied for a maximum value achieved from (5).

The second stage consists of two coupled-line QHCs (QHC2) and a $\lambda/8$ coplanar TL for 45° phase shifting. The last stage is another coupled-line QHC (QHC3) directly connected to the antenna port. Fig. 8(a) shows a coupled-line QHC and its simplified cross-sectional view. The even (Z_{0e}) and odd (Z_{0o}) impedances of the coupled line must satisfy the shown equations for the desired coupling (C) and characteristic impedance Z_0. A $\lambda/4$ coupled–coupled line with $C = \sqrt{2}/2$ is considered as a conventional coupled-line QHC. However, as depicted in Fig. 8(b), a higher coupling factor can be employed to decrease the required length in the cost of bandwidth. QHC2 is implemented with 5-μm width and 1-μm spacing to maximize the coupling (0.792), thus minimizing the length (420 μm). Even though the aluminum layer is used to increase the current handling of the QHCs, a wider width (10 μm) is chosen for the last QHC to address the reliability of the peak current at the wc VSWR. This feature leads to a lower coupling (0.753) and, thus, a longer length (540 μm) than QHC2.

Fig. 9 exhibits the simulated performance of the proposed eight-way power combiner, excluding the baluns. The

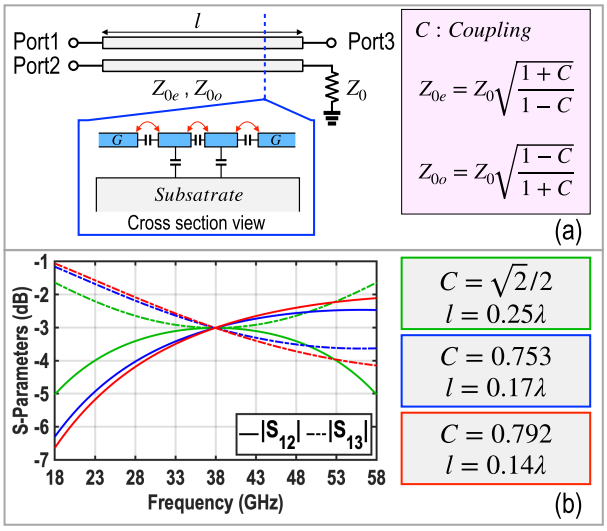

Fig. 8. (a) Coupled-line-based QHC and its cross-sectional view. (b) Simulated $|S_{12}|$ and $|S_{13}|$ of the coupled-line-based QHCs with different couplings.

S-parameter components of the output to each PA are demonstrated in Fig. 9(a). Since the characteristic impedance of all QHCs and TLs are 50 Ω, assuming a 50-Ω output load, the combiner provides a broadband 50-Ω loading condition for the PAs, as shown in Fig. 9(b). Moreover, the simulated group delay from each PA to the output is plotted in Fig. 9(c). Since QHC as a two-way combiner has an identical group delay, the pairs connected to the QHC1s have almost equal group delay. The group delay is separated by almost 1.64 ps, equal to 22.5° phase shift at 38 GHz. Finally, the combining gain of the

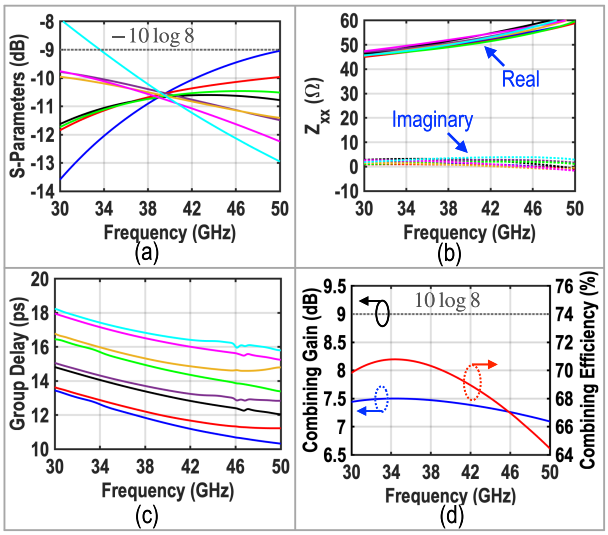

Fig. 9. (a) Simulated S-parameter components ($|S_{9n}|$) of the output (Port9) to each PAs (Port1–Port8). (b) Real and imaginary parts of the impedance seen by the PAs versus carrier frequency. (c) Simulated group delay from each PA to the output. (d) Combining gain and efficiency of the proposed eight-way power combiner. The output balun loss of the PAs is excluded in these simulation results.

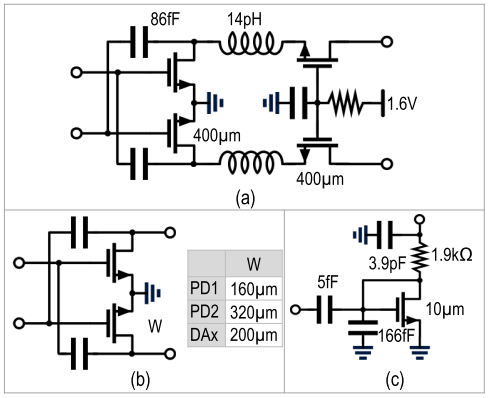

Fig. 10. Schematic of (a) PA, (b) driving amplifier and PDs, and (c) rms DET.

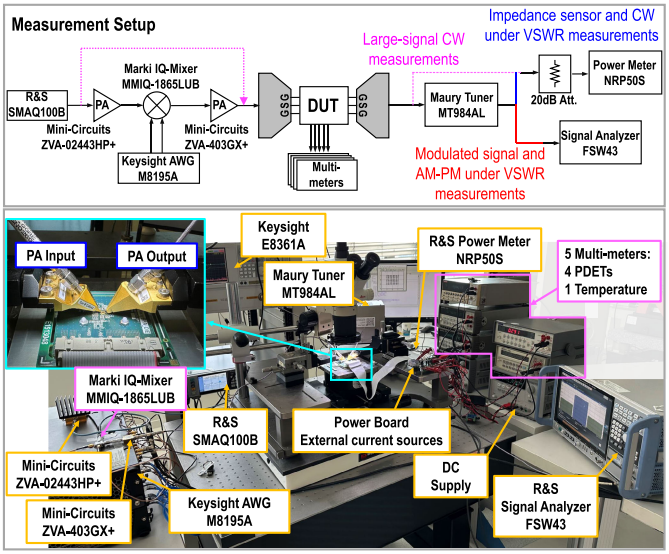

Fig. 11. Simplified CW and modulation measurement setups.

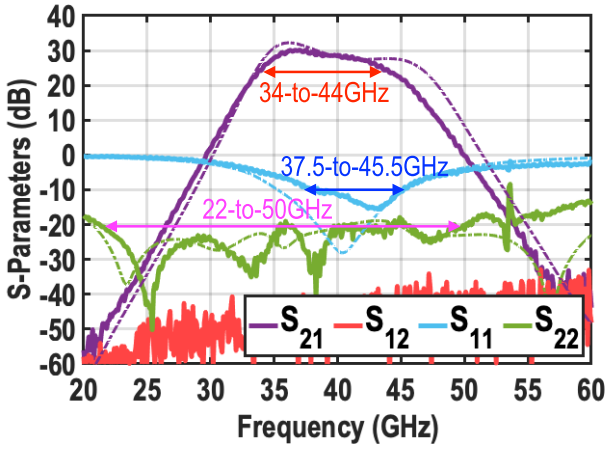

Fig. 12. S-parameter measurement (solid) and simulation (dashed) results of the proposed chain-weaver BPA.

proposed eight-way power combiner is depicted in Fig. 9(d), which is 1.5–1.9 dB less than 10 log 8.

The eight PA units comprise a common-source drive amplifier (DA) and a cascode PA. As shown in Fig. 10(a), two series inductors (14 pH) are utilized to improve PAE and gain [53]. In addition, the common-source pair is neutralized in all amplifiers to improve stability and boost power gain [see Fig. 10(b)]. Also, double-tuned transformers are designed as input, inter-stage, and output-matching networks to cover the targeted bandwidth. Also, four rms DETs are employed at the input of the second stage for impedance/power sensing. As depicted in Fig. 10(c), each DET comprises a capacitive coupler and a diode-connected nMOS biased at the weak inversion region with an external current source [54], [55].

VI. Measurement Results—Part I: Chain-Weaver BPA

All measurements are performed using a high-frequency probe station. The dc supplies, bias voltages, and rms DET pads are wire-bonded directly to an FR4 printed circuit board (PCB). Fig. 11 exhibits the continuous-wave (CW) and modulated signal measurement setups. In this work, 2-V supply voltage is used for the PAs and 1 V for the driver and PD amplifiers. A Maury MT984AL load tuner is used for the VSWR measurement. The tuner is characterized at the tip of the probe. The insertion losses of the probes and cables are measured and de embedded. The tuner loss variation as a function of VSWR at all operating frequencies is extracted and de-embedded.

A. 50-Ω Load Measurement Results

The small-signal S-parameter performance is measured using the Keysight E8361A network analyzer. As demonstrated in Fig. 12, the PA achieves 10-GHz small-signal $BW_{3\,dB}$, while its S_{22} is better than −20 dB in the 22–50-GHz band. The PA offers 29.9-dB small-signal gain at 37 GHz. Note that the bandwidth of the PA is mainly determined by the bandwidth of the double-tuned input, inter-stage, and output transformers utilized in the PDs, drive, and PAs.

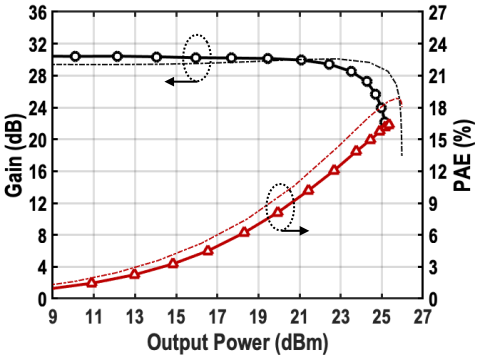

Fig. 13. Large-signal CW measurement (solid) and simulation (dashed) results at 37 GHz.

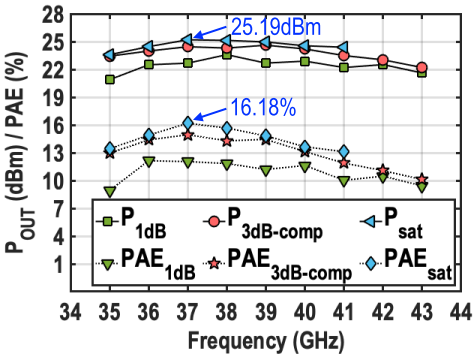

Fig. 14. Measured output power and PAE at 1-, 3-, and 6-dB gain compression point.

The large-signal CW measurement results at 37 GHz are reported in Fig. 13, where the PA achieves a saturated power (6-dB gain compression level) of 25.19 dBm and a PAE of 16.18%. Moreover, as shown in Fig. 14, the PA provides more than 22-dBm $P_{1\,\mathrm{dB}}$ over the 36–42-GHz band.

Wideband modulated signals, such as "64-QAM OFDM" and "256-QAM OFDM," verify the PA dynamic performance. Fig. 15(a) and (b) exhibits measured constellations and spectra of a 2-GHz "64-QAM OFDM" signal at 37- and 39-GHz carrier frequencies. Without digital pre-distortion (DPD), the PA achieves almost −25-dB EVM with 16- and 14.8-dBm average power at 37 and 39 GHz, respectively. The PA supports 800-MHz "256-QAM OFDM" signals with EVM ≅ −30.5 dB and average output powers of 11.8 and 10.8 dBm at 38 and 40 GHz, respectively.

The average power of a 100-MHz "64-QAM OFDM" signal versus carrier frequency is shown in Fig. 16 for EVM of −25, −30.5, and −35 dB. Besides, Fig. 17 demonstrates the measured EVM/ACLRs of a 50-MHz "64-QAM OFDM" signal versus the average power at 38 GHz.

B. VSWR Measurment Results

As discussed in Section II, linearity, gain, and output power robustness under load mismatch are crucial in mm-wave phased-array systems. The VSWR resilience of the proposed PA is evaluated by measuring its AM–PM and large-signal performance under VSWR. The Maury tuner was characterized at the probe tip, and its calibration was done as described in [36]. Since the angle of the load provided by the tuner varies considerably even in bandwidth as narrow as 50 MHz, the wideband modulation performance under VSWR will not accurately determine the resilience of the PA. Therefore, we report the linearity, gain, and output power variation under various VSWR conditions at different carrier frequencies to ensure that the PA supports wideband modulation signals under any VSWR condition.

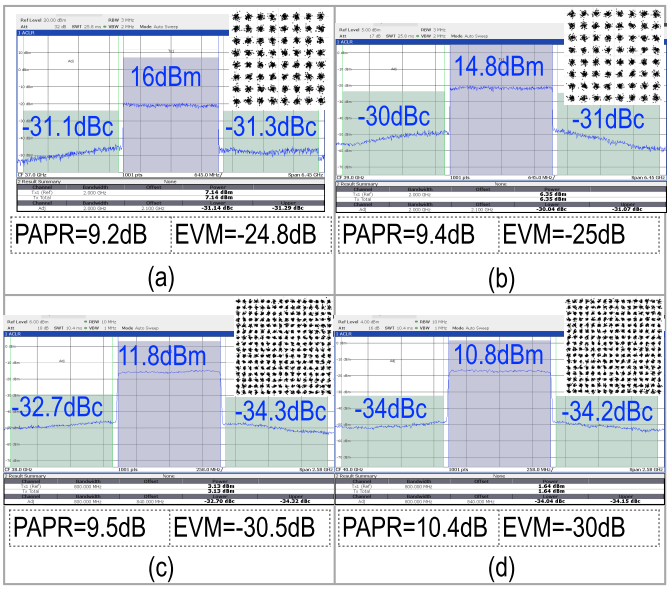

Fig. 15. Measured constellation and spectra of a 64-QAM OFDM signal with 2-GHz modulation bandwidth at (a) 37 GHz and (b) 39 GHz. Measured constellation and spectra of a 256-QAM OFDM signal with 800-MHz modulation bandwidth at (c) 38 GHz and (d) 40 GHz.

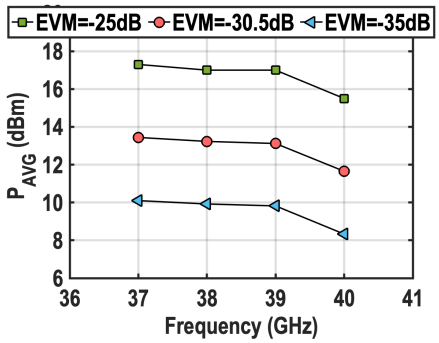

Fig. 16. Average power of a 64-QAM OFDM signal with 100-MHz modulation bandwidth versus carrier frequency when the measured EVMs are −25, −30.5, and −35 dB.

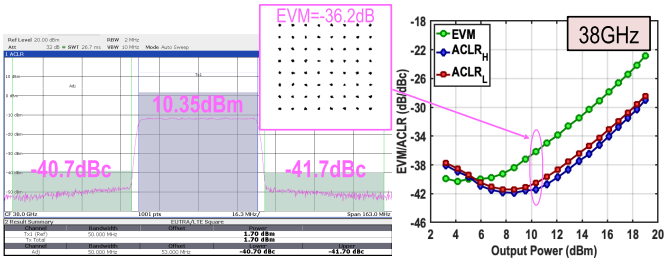

Fig. 17. Measured EVM/ACLRs versus average power at 38 GHz for a 50-MHz 64-QAM OFDM signal with PAPR = 8.6 dB.

TABLE I
SILICON-BASED mm-WAVE PAs' PERFORMANCE COMPARISON

			Mm-Wave 5G PAs				Efficiency Enhanced PAs/TXs				
Parameter	**This Work**		Zeng ISSCC 2023	Wang ISSCC 2020	Ahn RFIC 2020	Dasgupta RFIC 2019	Qunaj ISSCC 2021	Pashaeifar JSSC 2021	Mannem ISSCC 2020	Chappidi VLSI 19	Zhu ISSCC 2024
Architecture	**Chain-Weaver Eight-Way Balanced PA**		Two-Stage PA with Feedback Linearity	Compensated Distributed Balun	Eight-Way Power Combiner	Four-way DAT based Combiner	Doherty-Like LMBA	TX with Doherty Balanced PA	Reconfigurable Doherty PA	Broadband Doherty PA	Seven-Way LMBA
Technology	**40nm CMOS**		28nm CMOS	45nm SOI	65nm CMOS	65nm CMOS	28nm CMOS	40nm CMOS	45nm SOI	65nm CMOS	65nm CMOS
Core Area (mm^2)	**2.08**		0.106	0.21	0.25	0.945	1.44 (Die size)	1.38	1.18	1.35 (Die size)	2.2
Supply (V)	**1 (PDs + DA), 2 (PA)**		0.9, 1.8	2	NR	2.2	1	1	1, 2	1.1	1
Frequency (GHz)	**35 to 43**		19.7 to 43.8	25.8 to 43.4	28	39	36	24 to 30	39	26 to 42	27.8 to 38.3
Gain (dB)	**29.9 (37GHz)**		20.5	18.9 (37GHz)	15.9	38	18	21.8 (TX gain)	12.4*	13.5*	16.1 (38GHz)
P_{1dB} (dBm)	**22.67 (37GHz)**		17.6 (37GHz)	18.9 (37GHz)	22	21.5	19.6	20	20.2	19.2 (33GHz)	20 (38GHz)
P_{sat} (dBm)	**25.19 (37GHz)**		19.3 (37GHz)	20 (37GHz)	23.2	26	22.6	NA	20.8	19.6 (33GHz)	24.1 (38GHz)
PAE_{sat} (%)	**16.18 (37GHz)**		27	38.7 (37GHz)	33.5	26.6	32	31	33.3	24 (33GHz)	28.8 (38GHz)
S22 (dB)	**<-20**		-3.5~-4*	-1*	-5.8	-19*	-12*	-22.2	-9*	NA	<-20
$\frac{P_{sat} \times Gain \times PAE_{sat}}{Area}$	**80.6**		229.6	162.4	174.6	890.1	32.1	22.5	14.1	7.7	21.5
Modulation Bandwidth (GHz)	2	0.8	0.2	0.8	0.1	0.05	3	0.8	0.5	2	0.75
Modulation	**OFDM 64-QAM**	**OFDM 256-QAM**	OFDM 64-QAM	OFDM 64-QAM	256-QAM	OFDM 64-QAM	64-QAM	OFDM 64-QAM	64-QAM	OFDM 64-QAM	64-QAM
EVM_{rms} (dB)	**-25**	**-30.3**	-25.1 (37GHz)	-25.1	-31.2	-32*	-25.1	-27.1	-22.9	-24 (37GHz)	-26.1 (38GHz)
ACLR (dBc)	**-30.7**	**-33.3**	-24.1 (37GHz)	-27.8	-30	-33	NA	-32	-25.4	-25 (37GHz)	-31.1 (38GHz)
P_{avg} (dBm)	**16**	**12.17**	8.7 (37GHz)	10.2	18.2	14.7	15.5	8.4	12.2	10.2 (37GHz)	19.2 (38GHz)
PAEavg (%)	**4.1**	**1.93**	5.4 (37GHz)	13.6	17.6	NA	20	10.8#	16.1	9.8 (37GHz)	18.2 (38GHz)
VSWR	**1.5:1 to 3:1 @37 to 40GHz**		NA	NA	NA	NA	NA	3:1 @27 and 28GHz	3:1	4:1	NA
Gain Deviation (dB)	**0.7**		NA	NA	NA	NA	NA	0.65	0.9~1.3*	NA	NA
P_{1dB} Deviation (dB)	**0.79**		NA	NA	NA	NA	NA	NA	0.3~0.4*	~1*	NA
AM-PM_{max} (°)	**2.80**		NA	NA	NA	NA	NA	NA	NA	NA	NA

*Graphically estimated #PA drain efficiency.

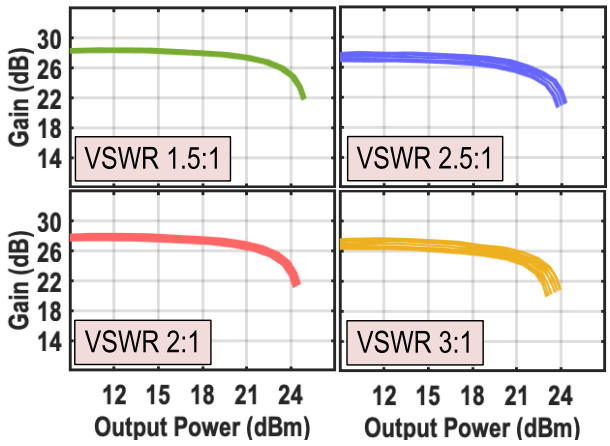

Fig. 18. Measured gain versus output power under VSWR at 37 GHz.

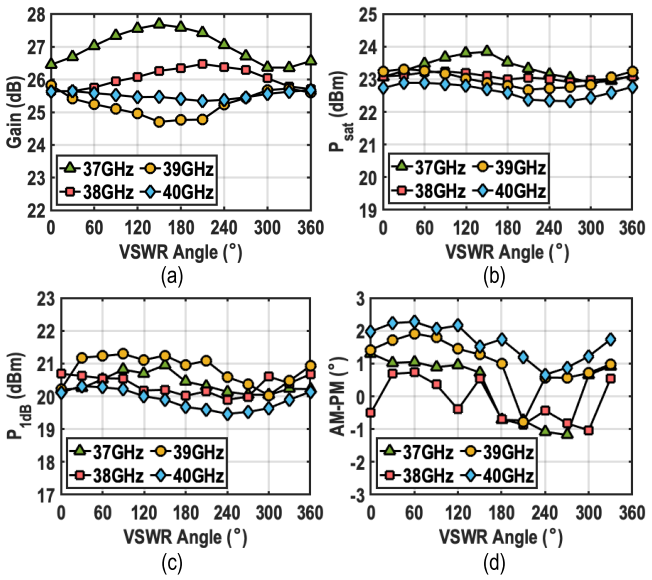

Fig. 19. (a) Gain and (b) saturated power, (c) $P_{1\,dB}$, and (d) AM–PM variation under VSWR 3:1.

Fig. 18 demonstrates the measured gain versus output power under various VSWRs at 37 GHz. The small-signal gain variation under VSWR 3:1 is ±0.7 dB. The gain and saturated power of the PA in the 37–40-GHz band are depicted in Fig. 19. Please note that the measured gain and power include 1.249-dB reflection loss $(1 - |\Gamma|^2)$.

Moreover, Fig. 20 exhibits the measured AM–PM under various VSWRs at 37 GHz. The normalized input 1-dB compression point power deviation is also shown in Fig. 20. Compared with the measured AM–PM shown in Fig. 1(b), the proposed chain-weaver BPA provides a robust linearity performance under VSWR. Lately, the measured AM–PM deviations under various VSWRs in the 37–40-GHz band are summarized in Fig. 21. It shows that in a 3-GHz bandwidth, the PA offers AM–PM <2.8° for any loading condition in the VSWR 3:1 circle.

Table I summarizes the proposed chain-weaver BPA's measured performance compared to the prior works. The chain-weaver BPA achieves notably high gain and $P_{1\,dB}$ thanks to its four-stage architecture and eight-way combing network, which increased its core area. For a better comparison of the performance considering the power/gain and area tradeoff, $((P_{sat} \times \text{Gain} \times \text{PAE}_{sat})/\text{Area})$ [W/mm^2] is also introduced in Table I.

VII. MEASUREMENT RESULTS—PART II: IMPEDANCE/POWER SENSOR

The performance of the embedded impedance/power sensor is evaluated under VSWR. As mentioned in Section IV, the

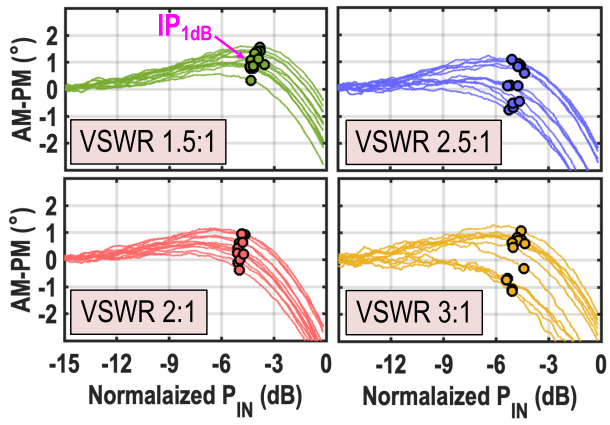

Fig. 20. Measured AM–PM versus output power under VSWR at 37 GHz.

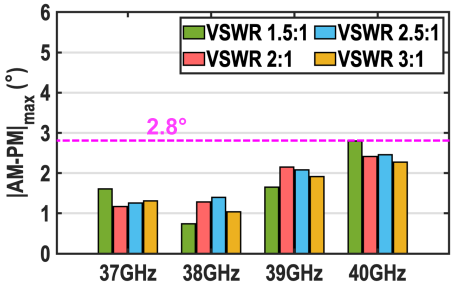

Fig. 21. Measured AM–PM deviation under VSWR 1.5:1–3:1 in the 37–40-GHz band.

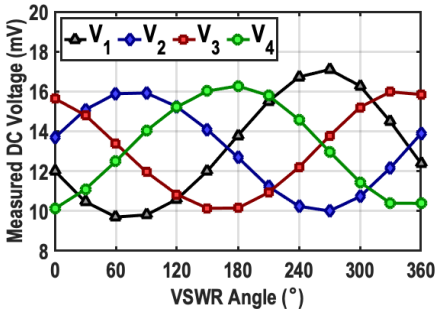

Fig. 22. Raw measured rms voltages at 40 GHz and 16-dBm output power.

measured voltage is not equal due to insertion loss mismatches, non-ideal output matching, parasitics at the output pad, or rms DET mismatch. Therefore, one-time calibration is required. First, the outputs of the rms DET are measured, while PA delivers a CW signal to a matched load (50 Ω). We then equalized them to have the same values for all four DETs in the matched loading condition. Furthermore, fixed magnitude and phase correction factors are applied at each carrier frequency to address the insertion loss and phase misalignment. In addition, the coupling ratio of the rms DET must be de-embedded for the actual power sensing. Fig. 22 shows the measured raw data at 40 GHz and 16-dBm output power under VSWR 3:1. As expected from (6), the measured rms voltages (V_{1-4}^2) vary with ∼90° phase difference. Here, (7)–(9) are utilized to calculate the magnitude and angle of the load impedance, and the output power.

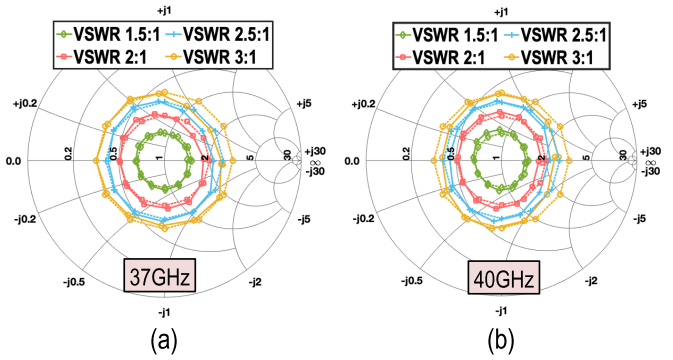

Fig. 23. Measured load reflection coefficients (solid line) and the tuner's configured load (dashed line).

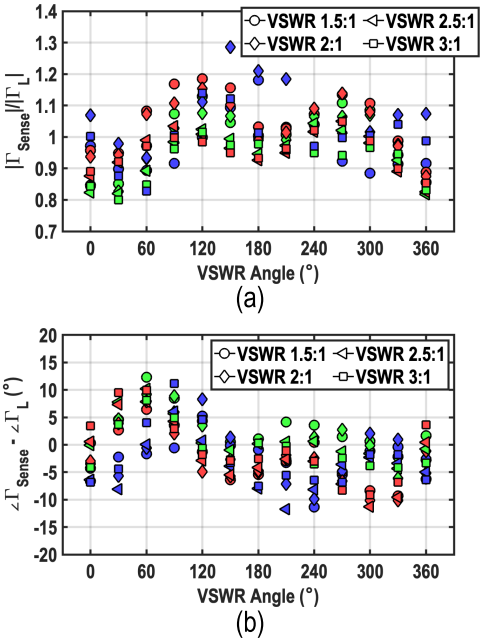

Fig. 24. Measured load (a) magnitude and (b) angle errors at 37 GHz (green), 38 GHz (blue), and 40 GHz (red).

Fig. 23 compares the measured load reflection coefficients (solid line) with the tuner's configured load (dashed line). To show the accuracy of the impedance sensor, the magnitude and angle error of the measured impedance are demonstrated in Fig. 24. We define the magnitude and angle error as

$$M_{\text{Error}} = \frac{|\Gamma_{\text{Sense}}|}{|\Gamma_L|} \tag{11}$$

$$\angle\Gamma_{\text{Error}} = \angle\Gamma_{\text{Sense}} - \angle\Gamma_L \tag{12}$$

where Γ_L is the load provided by the tuner and Γ_{Sense} is the load measured by the impedance sensor. The magnitude error is evaluated by its ratio rather than its difference to ensure reasonably high accuracy for all VSWR conditions. Fig. 24(a) shows the maximum error occurs at 38 GHz for VSWR 2:1 and 150° ($M_{\text{Error}} = 1.286$), while the maximum angle error observed at 37 GHz for VSWR 1.5:1 at 60° ($\angle\Gamma_{\text{Error}} = 12.3°$).

Thus far, the impedance sensor accuracy has been examined at one output power level. However, since the impedance of the PA can change by its output power, it may impact the accuracy of the impedance sensor. Therefore, the measured $|\Gamma_{\text{Sense}}|$ and

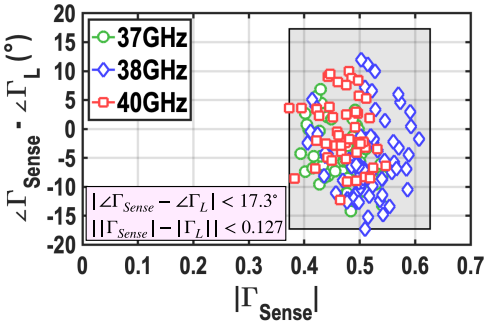

Fig. 25. Measured $\angle\Gamma_{\text{Error}}$ versus $|\Gamma_{\text{Sense}}|$ for VSWR 3:1 (VSWR angle = 0°:30°:360°) at five different output powers with 2-dB step.

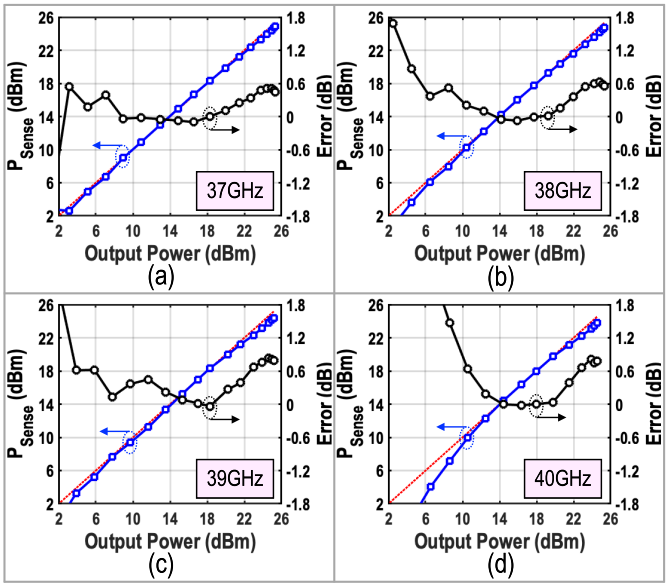

Fig. 26. Measured output power using the embedded power sensor and its error ($P_{\text{OUT}} - P_{\text{Sense}}$) at (a) 37 GHz, (b) 38 GHz, (c) 39 GHz, and (d) 40 GHz.

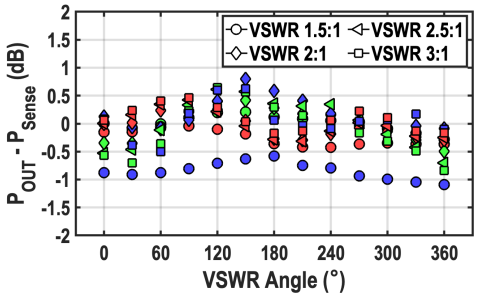

Fig. 27. Power-sensing error under VSWR at 37 GHz (green), 38 GHz (blue), and 40 GHz (red).

$\angle\Gamma_{\text{Error}}$ for VSWR 3:1 (VSWR angle = 0°:30°:360°) at five different output powers with 2-dB step are depicted in Fig. 25. It shows that the impedance sensor can measure VSWR 3:1 by the maximum angle and magnitude errors of 17.3° and 0.127°, respectively.

As explained in Section IV, the output power can be calculated using (9). We first measured the output power for a 50-Ω matched load. Fig. 26 exhibits the measured output power using the embedded power sensor and its error ($P_{\text{OUT}} - P_{\text{Sense}}$) versus the output power (P_{OUT}) measured by an external power meter. The power sensor is calibrated one time at 18-dBm output power. The power-sensing error under VSWR at different carrier frequencies is also demonstrated in Fig. 27. The maximum error is −1.092 dB, which occurs at 38 GHz.

TABLE II
IMPEDANCE SENSORS' PERFORMANCE COMPARISON

		Mm-Wave/RF Impedance Sensors			
Parameter	**This Work**	Munzer ISSCC 2022	Zhang ISSCC 2021	Munzer MWCL 2021	Lu ISSCC 2017
Technology	**40nm CMOS**	45nm SOI	22nm SOI	45nm SOI	40nm CMOS
VSWR	**1.5:1 to 3:1**	3	3	3	3
Frequency (GHz)	**37 to 40**	27 to 41	28	38	2.4
$\lvert 20\log\frac{\lvert\Gamma_{Sense}\rvert}{\lvert\Gamma_L\rvert}\rvert(dB)$	**2.14**	2.38 (Estimated)	NA	3.38	1.87 (Estimated)
$\lvert\lvert\Gamma_{Sense}\rvert - \lvert\Gamma_L\rvert\rvert$	**0.106**	0.149 (37GHz)	0.14	0.238	0.1
$\lvert\angle\Gamma_{Sense} - \angle\Gamma_L\rvert(°)$	**12.3**	18.72 (37GHz)	33	28.9	18

VIII. CONCLUSION

This article presented an N-way chain-weaver BPA for mm-wave phased-array TXs. The proposed PA architecture offers linearity and gains robustness under frequency/time-dependent VSWR, while it comprises an embedded impedance/power sensor. In the event of VSWR, the proposed PA provides N different loads distributed on the VSWR circle with equal angle distance. An eight-way chain-weaver BPA is realized in 40-nm bulk CMOS technology as a proof of concept. The proposed PA supports a 2-GHz 64-QAM OFDM signal with 16-dBm average power. Assuming any frequency/time-dependent loading condition within the VSWR 3:1 circle, the proposed chain-weaver BPA achieves <2.8° AM–PM over 3-GHz BW. Finally, as compared in Table II, the proposed embedded impedance/power sensor accuracy surpasses the best-in-class companions.

APPENDIX

Assuming no IQMM in the QHC, a perfect reflected signal cancellation was considered in Sections III and IV. However, the IQMM of the QHC can lead to additional combining power loss, power leaking into the termination resistors, and non-perfect output matching, which can introduce gain variation and degrade the accuracy of the proposed impedance/power sensor.

Fig. 28 depicts a simplified conventional BPA assuming a QHC with ϵ and $\Delta\theta$ as its amplitude and phase errors, respectively. Following the same notation as in Fig. 4, we have $V_{f1} = V_{\text{tx}}\angle 0°$ and $V_{f2} = V_{\text{tx}}\angle 90°$. Therefore, the output forward signal and the termination resistor voltage can be obtained by

$$V_{f\text{-out}} = V_{\text{tx}} \cdot \text{IL}_{\text{QHC}} \cdot \sqrt{1 + \frac{2(1+\epsilon)\cos\Delta\theta}{1+(1+\epsilon)^2}} \tag{13}$$

$$V_{\text{term}} = V_{\text{tx}} \cdot \text{IL}_{\text{QHC}} \cdot \sqrt{1 - \frac{2(1+\epsilon)\cos\Delta\theta}{1+(1+\epsilon)^2}} \tag{14}$$

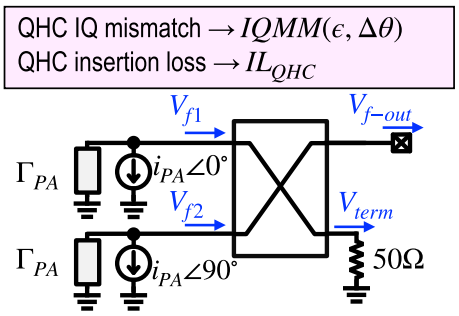

Fig. 28. Simplified BPA operating in the presence of QHC IQ mismatch.

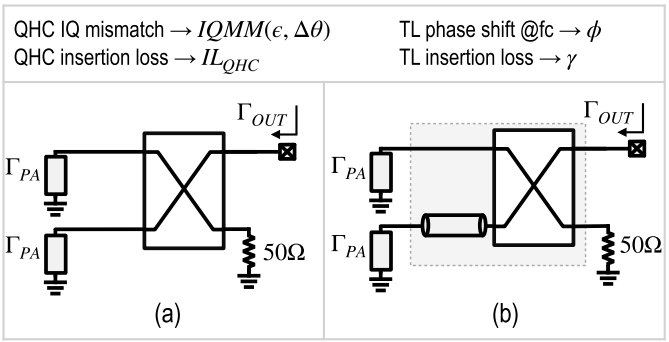

Fig. 29. (a) Simplified BPA representing the first stage of the chain-weaver PA. (b) BPA with an additional TL representing the second and third stages of the chain-weaver PA.

where IL_{QHC} is the insertion loss of the QHC. Therefore, contrary to the reliability criteria posed by VSWR for the first-stage termination resistors, the reliability of the second and third stages is more at risk due to higher power levels. Hence, all termination resistors' reliability must be satisfied for the maximum possible amplitude/phase errors and peak power.

An imperfect QHC deteriorates the reflected signal cancellation in a BPA and, as a result, degrades the output-matching condition. In a conventional BPA as exhibited in Fig. 29(a), the output reflection coefficient (Γ_{OUT}) can be calculated as

$$|\Gamma_{OUT}| = \frac{\sqrt{1+(1+\epsilon)^4-2(1+\epsilon)^2\cos 2\Delta\theta}}{1+(1+\epsilon)^2}|\Gamma_{PA}|\cdot|IL_{QHC}|^2 \quad (15)$$

which explains the gain variation illustrated in Fig. 3(c).

To extend this analysis to the proposed chain-weaver PA, we need to consider added TLs' insertion losses and phase shifts, as shown in Fig. 29(b). Assuming that TL phase shift and insertion loss are ϕ and γ, respectively, the output reflection coefficient can be calculated as

$$|\Gamma_{OUT}| = \frac{\sqrt{1+\hat{\gamma}^4-2\hat{\gamma}^2\cos 2\Delta\hat{\theta}}}{1+\hat{\gamma}^2}|\Gamma_{PA}|\cdot|IL_{QHC}|^2 \quad (16)$$

where $\hat{\gamma}=\gamma(1+\epsilon)$ and $\Delta\hat{\theta}=\Delta\theta+\phi$. Now, by replacing $|\Gamma_{PA}|$ in the above equation with an expression from the previous formula and considering $\phi = 22.5°$, we can obtain the output reflection coefficient of the second stage. Likewise, the calculated coefficient can be employed in (16) again, this time considering $\phi = 45°$, to obtain the output coefficient of the eight-way chain-weaver PA.

ACKNOWLEDGMENT

The author would like to thank imec, Leuven, Belgium, for handling the tape-out. They also like to thank Atef Akhnoukh, Zu-Yao Chang, and Dr. Juan Bueno Lopez for their strong support during the design, fabrication, and measurement.

REFERENCES

[1] P. M. Asbeck, N. Rostomyan, M. Özen, B. Rabet, and J. A. Jayamon, "Power amplifiers for mm-wave 5G applications: Technology comparisons and CMOS-SOI demonstration circuits," *IEEE Trans. Microw. Theory Techn.*, vol. 67, no. 7, pp. 3099–3109, Jul. 2019.

[2] T. Tuovinen, N. Tervo, and A. Pärssinen, "Analyzing 5G RF system performance and relation to link budget for directive MIMO," *IEEE Trans. Antennas Propag.*, vol. 65, no. 12, pp. 6636–6645, Dec. 2017.

[3] B. Sadhu et al., "A 28-GHz 32-element TRX phased-array IC with concurrent dual-polarized operation and orthogonal phase and gain control for 5G communications," *IEEE J. Solid-State Circuits*, vol. 52, no. 12, pp. 3373–3391, Dec. 2017.

[4] M. Pashaeifar, L. C. N. De Vreede, and M. S. Alavi, "A millimeter-wave front-end for FD/FDD transceivers featuring an embedded PA and an N-path filter based circulator receiver," in *Proc. IEEE Radio Freq. Integr. Circuits Symp. (RFIC)*, Jun. 2022, pp. 11–14.

[5] M. Pashaeifar, L. C. N. de Vreede, and M. S. Alavi, "A millimeter-wave mutual-coupling-resilient double-quadrature transmitter for 5G applications," *IEEE J. Solid-State Circuits*, vol. 56, no. 12, pp. 3784–3798, Dec. 2021.

[6] D. Zhao and P. Reynaert, "A 40-nm CMOS E-band 4-way power amplifier with neutralized bootstrapped cascode amplifier and optimum passive circuits," *IEEE Trans. Microw. Theory Techn.*, vol. 63, no. 12, pp. 4083–4089, Dec. 2015.

[7] B. Park, D. Jeong, J. Kim, Y. Cho, K. Moon, and B. Kim, "Highly linear CMOS power amplifier for mm-wave applications," in *IEEE MTT-S Int. Microw. Symp. Dig.*, May 2016, pp. 1–3.

[8] S. Shakib, M. Elkholy, J. Dunworth, V. Aparin, and K. Entesari, "A wideband 28 GHz power amplifier supporting 8 × 100 MHz carrier aggregation for 5G in 40 nm CMOS," in *IEEE Int. Solid-State Circuits Conf. (ISSCC) Dig. Tech. Papers*, Feb. 2017, pp. 44–45.

[9] M. Vigilante and P. Reynaert, "A 29-to-57 GHz AM-PM compensated class-AB power amplifier for 5G phased arrays in 0.9 V 28 nm bulk CMOS," in *Proc. IEEE Radio Freq. Integr. Circuits Symp. (RFIC)*, Jun. 2017, pp. 116–119.

[10] T.-W. Li, S. Li, H. M. Lavasani, and H. Wang, "A V-band doubly hybrid NMOS/PMOS four-way distributed-active-transformer power amplifier for nonlinearity cancellation and joint linearity/efficiency optimization," in *IEEE MTT-S Int. Microw. Symp. Dig.*, Jun. 2021, pp. 382–385.

[11] S. Kulkarni and P. Reynaert, "A 60-GHz power amplifier with AM-PM distortion cancellation in 40-nm CMOS," *IEEE Trans. Microw. Theory Techn.*, vol. 64, no. 7, pp. 2284–2291, Jul. 2016.

[12] M. Abdulaziz, H. V. Hünerli, K. Buisman, and C. Fager, "Improvement of AM-PM in a 33-GHz CMOS SOI power amplifier using pMOS neutralization," *IEEE Microw. Wireless Compon. Lett.*, vol. 29, no. 12, pp. 798–801, Dec. 2019.

[13] W.-C. Huang, J.-L. Lin, Y.-H. Lin, and H. Wang, "A K-band power amplifier with 26-dBm output power and 34% PAE with novel inductance-based neutralization in 90-nm CMOS," in *Proc. IEEE Radio Freq. Integr. Circuits Symp. (RFIC)*, Jun. 2018, pp. 228–231.

[14] C.-W. Wu, Y.-H. Lin, Y.-H. Hsiao, C.-F. Chou, Y.-C. Wu, and H. Wang, "Design of a 60-GHz high-output power stacked-FET power amplifier using transformer-based voltage-type power combining in 65-nm CMOS," *IEEE Trans. Microw. Theory Techn.*, vol. 66, no. 10, pp. 4595–4607, Oct. 2018.

[15] E. C. Wagner and G. M. Rebeiz, "An 8-way combined E-band power amplifier with 24 dBm P_{sat} and 12% PAE in 0.12 μm SiGe," in *IEEE MTT-S Int. Microw. Symp. Dig.*, Jun. 2018, pp. 1342–1344.

[16] H.-C. Park et al., "A 39 GHz-band CMOS 16-channel phased-array transceiver IC with a companion dual-stream IF transceiver IC for 5G NR base-station applications," in *IEEE Int. Solid-State Circuits Conf. (ISSCC) Dig. Tech. Papers*, Feb. 2020, pp. 76–78.

[17] D. Manente, F. Padovan, D. Seebacher, M. Bassi, and A. Bevilacqua, "A 28-GHz stacked power amplifier with 20.7-dBm output P1dB in 28-nm bulk CMOS," *IEEE Solid-State Circuits Lett.*, vol. 3, pp. 170–173, 2020.

[18] H. Ahn, I. Nam, and O. Lee, "A 28-GHz highly efficient CMOS power amplifier using a compact symmetrical 8-way parallel-parallel power combiner with IMD3 cancellation method," in *Proc. IEEE Radio Freq. Integr. Circuits Symp. (RFIC)*, Aug. 2020, pp. 187–190.

[19] M. Pashaeifar, L. C. N. de Vreede, and M. S. Alavi, "Load-modulation-based IMD3 cancellation for millimeter-wave class-B CMOS power amplifiers achieving EVM < 1.2%," *IEEE Microw. Wireless Compon. Lett.*, vol. 32, no. 6, pp. 716–719, Jun. 2022.

[20] F. Wang and H. Wang, "A broadband linear ultra-compact mm-wave power amplifier with distributed-balun output network: Analysis and design," *IEEE J. Solid-State Circuits*, vol. 56, no. 8, pp. 2308–2323, Aug. 2021.

[21] W. Zeng, L. Gao, N. Sun, H. Xu, Q. Xue, and X. Zhang, "A 19.7-to-43.8 GHz power amplifier with broadband linearization technique in 28 nm bulk CMOS," in *IEEE Int. Solid-State Circuits Conf. (ISSCC) Dig. Tech. Papers*, Feb. 2023, pp. 372–374.

[22] H. Wang, P. M. Asbeck, and C. Fager, "Millimeter-wave power amplifier integrated circuits for high dynamic range signals," *IEEE J. Microw.*, vol. 1, no. 1, pp. 299–316, Jan. 2021.

[23] P. Taghikhani, K. Buisman, and C. Fager, "Hybrid beamforming transmitter modeling for millimeter-wave MIMO applications," *IEEE Trans. Microw. Theory Techn.*, vol. 68, no. 11, pp. 4740–4752, Nov. 2020.

[24] C. Fager, T. Eriksson, F. Barradas, K. Hausmair, T. Cunha, and J. C. Pedro, "Linearity and efficiency in 5G transmitters: New techniques for analyzing efficiency, linearity, and linearization in a 5G active antenna transmitter context," *IEEE Microw. Mag.*, vol. 20, no. 5, pp. 35–49, May 2019.

[25] F. M. Barradas, P. M. Tomé, J. M. Gomes, T. R. Cunha, P. M. Cabral, and J. C. Pedro, "Power, linearity, and efficiency prediction for MIMO arrays with antenna coupling," *IEEE Trans. Microw. Theory Techn.*, vol. 65, no. 12, pp. 5284–5297, Dec. 2017.

[26] S. K. Dhar, A. Abdelhafiz, M. Aziz, M. Helaoui, and F. M. Ghannouchi, "A reflection-aware unified modeling and linearization approach for power amplifier under mismatch and mutual coupling," *IEEE Trans. Microw. Theory Techn.*, vol. 66, no. 9, pp. 4147–4157, Sep. 2018.

[27] X. Chen, S. Zhang, and Q. Li, "A review of mutual coupling in MIMO systems," *IEEE Access*, vol. 6, pp. 24706–24719, 2018.

[28] X. Chen, M. Abdullah, Q. Li, J. Li, A. Zhang, and T. Svensson, "Characterizations of mutual coupling effects on switch-based phased array antennas for 5G millimeter-wave mobile communications," *IEEE Access*, vol. 7, pp. 31376–31384, 2019.

[29] S. M. Bowers, K. Sengupta, K. Dasgupta, B. D. Parker, and A. Hajimiri, "Integrated self-healing for mm-wave power amplifiers," *IEEE Trans. Microw. Theory Techn.*, vol. 61, no. 3, pp. 1301–1315, Mar. 2013.

[30] N. S. Mannem, M.-Y. Huang, T.-Y. Huang, and H. Wang, "A reconfigurable hybrid series/parallel Doherty power amplifier with antenna VSWR resilient performance for MIMO arrays," *IEEE J. Solid-State Circuits*, vol. 55, no. 12, pp. 3335–3348, Dec. 2020.

[31] C. R. Chappidi, X. Wu, and K. Sengupta, "Simultaneously broadband and back-off efficient mm-wave PAs: A multi-port network synthesis approach," *IEEE J. Solid-State Circuits*, vol. 53, no. 9, pp. 2543–2559, Sep. 2018.

[32] T. Dinc, A. Nagulu, and H. Krishnaswamy, "A millimeter-wave non-magnetic passive SOI CMOS circulator based on spatio-temporal conductivity modulation," *IEEE J. Solid-State Circuits*, vol. 52, no. 12, pp. 3276–3292, Dec. 2017.

[33] A. Nagulu and H. Krishnaswamy, "28.5 non-magnetic 60 GHz SOI CMOS circulator based on loss/dispersion-engineered switched bandpass filters," in *IEEE Int. Solid-State Circuits Conf. (ISSCC) Dig. Tech. Papers*, Feb. 2019, pp. 446–448.

[34] Y. Zhang, G. Mangraviti, J. Nguyen, Z. Zong, and P. Wambacq, "A reflection-coefficient sensor for 28 GHz beamforming transmitters in 22 nm FD-SOI CMOS," in *IEEE Int. Solid-State Circuits Conf. (ISSCC) Dig. Tech. Papers*, vol. 64, Feb. 2021, pp. 360–362.

[35] D. Munzer, N. S. Mannem, E. F. Garay, and H. Wang, "Single-ended quadrature coupler-based VSWR resilient joint mm-wave true power detector and impedance sensor," *IEEE Trans. Microw. Theory Techn.*, vol. 70, no. 5, pp. 2802–2814, May 2022.

[36] D. Munzer, N. S. Mannem, J. Lee, and H. Wang, "Broadband mm-wave current/voltage sensing-based VSWR-resilient true power/impedance sensor supporting single-ended antenna interfaces," *IEEE J. Solid-State Circuits*, vol. 58, no. 6, pp. 1535–1551, Jun. 2023.

[37] E. Liu, D. Munzer, J. Lee, and H. Wang, "A compact broadband VSWR-resilient true-power-and-gain sensor with dynamic-range compensation for phased-array applications," in *IEEE Int. Solid-State Circuits Conf. (ISSCC) Dig. Tech. Papers*, Feb. 2024, pp. 538–540.

[38] M. Pashaeifar, L. C. N. de Vreede, and M. S. Alavi, "A 24-to-30 GHz double-quadrature direct-upconversion transmitter with mutual-coupling-resilient series-Doherty balanced PA for 5G MIMO arrays," in *IEEE Int. Solid-State Circuits Conf. (ISSCC) Dig. Tech. Papers*, vol. 64, Feb. 2021, pp. 223–225.

[39] M. Pashaeifar, A. K. Kumaran, L. C. N. De Vreede, and M. S. Alavi, "A 25.2 dBm P_{SAT}, 35-to-43 GHz VSWR-resilient chain-weaver eight-way balanced PA with an embedded impedance/power sensor," in *IEEE Int. Solid-State Circuits Conf. (ISSCC) Dig. Tech. Papers*, Feb. 2024, pp. 532–534.

[40] A. Verma et al., "A 16-channel, 28/39 GHz dual-polarized 5G FR2 phased-array transceiver IC with a quad-stream IF transceiver supporting non-contiguous carrier aggregation up to 1.6 GHz BW," in *IEEE Int. Solid-State Circuits Conf. (ISSCC) Dig. Tech. Papers*, vol. 65, Feb. 2022, pp. 1–3.

[41] H.-T. Kim et al., "A 28-GHz CMOS direct conversion transceiver with packaged 2 × 4 antenna array for 5G cellular system," *IEEE J. Solid-State Circuits*, vol. 53, no. 5, pp. 1245–1259, May 2018.

[42] F. Wang and H. Wang, "A high-power broadband multi-primary DAT-based Doherty power amplifier for mm-wave 5G applications," *IEEE J. Solid-State Circuits*, vol. 56, no. 6, pp. 1668–1681, Jun. 2021.

[43] M. Pashaeifar, A. K. Kumaran, M. Beikmirza, L. C. N. de Vreede, and M. S. Alavi, "A 24-to-32 GHz series-Doherty PA with two-step impedance inverting power combiner achieving 20.4 dBm P_{sat} and 38%/34% PAE at P_{sat}/6 dB PBO for 5G applications," in *Proc. IEEE Asian Solid-State Circuits Conf. (A-SSCC)*, Nov. 2021, pp. 1–3.

[44] H. Oh et al., "A 24.25-to-29.5 GHz extremely compact Doherty power amplifier with differential-breaking phase offset achieving 23.7% PAEavg for 5G base-station transceivers," in *ISSCC*, Feb. 2024, pp. 522–524.

[45] W. Zhu et al., "A 27.8-to-38.7 GHz load-modulated balanced power amplifier with scalable 7-to-1 load-modulated power-combine network achieving 27.2 dBm output power and 28.8%/23.2%/16.3%/11.9% peak/6/9/12 dB back-off efficiency," in *IEEE Int. Solid-State Circuits Conf. (ISSCC) Dig. Tech. Papers*, Feb. 2024, pp. 534–536.

[46] A. K. Kumaran, M. Pashaeifar, M. Alexanderson, L. C. N. D. Vreede, and M. S. Alavi, "A single-supply balun-first three-way mm-wave Doherty PA," *IEEE Trans. Microw. Theory Techn.*, vol. 72, no. 5, pp. 2757–2772, May 2024.

[47] J. D. Dunworth et al., "A 28 GHz bulk-CMOS dual-polarization phased-array transceiver with 24 channels for 5G user and basestation equipment," in *IEEE Int. Solid-State Circuits Conf. (ISSCC) Dig. Tech. Papers*, Feb. 2018, pp. 70–72.

[48] Y. Yin, B. Ustundag, K. Kibaroglu, M. Sayginer, and G. M. Rebeiz, "Wideband 23.5–29.5-GHz phased arrays for multistandard 5G applications and carrier aggregation," *IEEE Trans. Microw. Theory Techn.*, vol. 69, no. 1, pp. 235–247, Jan. 2021.

[49] Y. Wang et al., "A 39-GHz 64-element phased-array transceiver with built-in phase and amplitude calibrations for large-array 5G NR in 65-nm CMOS," *IEEE J. Solid-State Circuits*, vol. 55, no. 5, pp. 1249–1269, May 2020.

[50] A. M. Darwish, A. A. Ibrahim, J. X. Qiu, E. Viveiros, and H. A. Hung, "A broadband 1-to-N power divider/combiner with isolation and reflection cancellation," *IEEE Trans. Microw. Theory Techn.*, vol. 63, no. 7, pp. 2253–2263, Jul. 2015.

[51] F. Torres, M. De Matos, A. Cathelin, and E. Kerhervé, "A 31 GHz 2-stage reconfigurable balanced power amplifier with 32.6 dB power gain, 25.5% PAEmax and 17.9 dBm P_{sat} in 28 nm FD-SOI CMOS," in *Proc. IEEE Radio Freq. Integr. Circuits Symp. (RFIC)*, Jun. 2018, pp. 236–239.

[52] S. Shahramian, M. J. Holyoak, A. Singh, and Y. Baeyens, "A fully integrated 384-element, 16-tile, W-band phased array with self-alignment and self-test," *IEEE J. Solid-State Circuits*, vol. 54, no. 9, pp. 2419–2434, Sep. 2019.

[53] H.-T. Dabag, B. Hanafi, F. Golcuk, A. Agah, J. F. Buckwalter, and P. M. Asbeck, "Analysis and design of stacked-FET millimeter-wave power amplifiers," *IEEE Trans. Microw. Theory Techn.*, vol. 61, no. 4, pp. 1543–1556, Apr. 2013.

[54] S. Kshattry, W. Choi, C. Yu, and K. O. Kenneth, "Compact diode connected MOSFET detector for on-chip millimeter-wave voltage measurements," *IEEE Microw. Wireless Compon. Lett.*, vol. 26, no. 5, pp. 349–351, May 2016.

[55] M. Pashaeifar, L. C. N. de Vreede, and M. S. Alavi, "A millimeter-wave CMOS series-Doherty power amplifier with post-silicon inter-stage passive validation," *IEEE J. Solid-State Circuits*, vol. 57, no. 10, pp. 2999–3013, Oct. 2022.

Masoud Pashaeifar (Member, IEEE) was born in Tabriz, Iran. He received the M.Sc. degree in circuits and systems from the University of Tehran, Tehran, Iran, in 2013. He is currently pursuing the Ph.D. degree with Delft University of Technology, Delft, The Netherlands.

He was the Head of the Hardware Research Group, Bakhtar Communication Company, Tehran, from 2014 to 2018. He has been with Apple Inc., Munich, Germany, since September 2022. His research interests include RF/millimeter-wave (mm-wave)/sub-THz transceivers.

Mr. Pashaeifar received the IEEE Solid-State Circuits Society Predoctoral Achievement Award for the term of 2021–2022. He serves as a reviewer for IEEE JOURNAL OF SOLID-STATE CIRCUITS, IEEE SOLID-STATE CIRCUITS LETTERS, and IEEE TRANSACTIONS ON CIRCUITS AND SYSTEMS—I: REGULAR PAPERS.

Anil Kumar Kumaran (Graduate Student Member, IEEE) received the B.Tech. degree in electronics and communication engineering from Amrita Vishwa Vidyapeetham, Coimbatore, India, in May 2015, and the M.Sc. degree in microelectronics from Delft University of Technology, Delft, The Netherlands, in August 2020, where he is currently pursuing the Ph.D. degree with the ELCA Research Group.

Before joining the master's degree, he was an Onsite Validation Engineer with Texas Instruments India, Bangalore, India. His research interests include designing linear and efficient millimeter-wave (mm-wave) transmitters for 5G cellular applications.

Leo C. N. de Vreede (Senior Member, IEEE) received the Ph.D. degree (cum laude) from Delft University of Technology, Delft, The Netherlands, in 1996.

In 1996, he was appointed as an Assistant Professor with Delft University of Technology, working on the nonlinear distortion behavior of active devices. He was appointed as an Associate and a Full Professor with Delft University of Technology, in 1999 and 2015, respectively, where he became responsible for the Electronic Research Laboratory (ERL/ELCA). During that period, he worked on solutions for improved linearity and RF performance at the device, circuit, and system levels. He is the Co-Founder/an Advisor of Anteverta-mw B.V., Eindhoven, The Netherlands, a company that is specialized in RF device characterization. He has (co-)authored more than 130 IEEE refereed conference papers and journal articles. He holds several patents. His current research interests include RF measurement systems, RF technology optimization, and (digital-intensive) energy-efficient/wideband circuit/system concepts for wireless applications.

Dr. de Vreede was a (co-)recipient of the IEEE Microwave Prize in 2008 and a Mentor of the Else Kooi Prize Awarded Ph.D. Work in 2010 and the Dow Energy Dissertation Prize Awarded Ph.D. Work in 2011. He was a recipient of the TUD Entrepreneurial Scientist Award in 2015. He (co-)guided several students that won (best) paper awards at the Bipolar/BiCMOS Circuits and Technology Meeting (BCTM), the Program for Research on Integrated Systems and Circuits (PRORISC), European Solid-state Circuits and Devices Conference (ESSDERC), the International Microwave Symposium (IMS), the Radio Frequency Integration Technology (RFIT), and the Radio Frequency Integrated Circuits Symposium (RFIC).

Morteza S. Alavi (Senior Member, IEEE) was born in Tehran, Iran. He received the B.S.E.E. degree from Iran University of Science and Technology, Tehran, in 2003, the M.S.E.E. degree from the University of Tehran, Tehran, in 2006, and the Ph.D. degree in electrical engineering from Delft University of Technology (TU-Delft), Delft, The Netherlands, in 2014.

He was the Co-Founder and the CEO of DitIQ B.V., Delft, a local company developing energy-efficient, wideband wireless transmitters for the next generation of the cellular network. Since September 2016, he has been with the Electronic Circuits and Architectures (ELCA) Research Group, TU-Delft, where he is currently a tenured Assistant Professor. He has co-authored the book *Radio-Frequency Digital-to-Analog Converter* (Elsevier, 2016). His main research interest is designing high-frequency and high-speed wireless/cellular communication and sensor systems, as well as in the field of wireline transceivers.

Dr. Alavi was the Best Paper Award recipient of the 2011 IEEE International Symposium on Radio-Frequency Integrated Technology (RFIT). He received the Best Student Paper Award (Second Place) at the 2013 Radio-Frequency Integrated Circuits (RFIC) Symposium. His Ph.D. student also won the Best Student Paper Award (First Place) of the 2017 RFIC Symposium held in Honolulu, HI, USA. His research group received the 2021 Institute of Semiconductor Engineers (ISE) President Best Paper Award of the International SoC Design Conference (ISOCC). He is a co-recipient of the 2022 Best Paper Award of the honorable mentioned IEEE Brain and SSCS Joint Communities paper.